INSTITUTE OF PHYSICS PUBLISHING PHYSICS IN MEDICINE AND BIOLOGY

Phys. Med. Biol. **51** (2006) 3015–3030 doi:10.1088/0031-9155/51/12/001

Experimental validation of a simple model capable of predicting the phase contrast imaging capabilities of any x-ray imaging system

A Olivo and R Speller

Department of Medical Physics and Bioengineering, University College of London, Malet Place, Gower Street, London WC1E 6BT, UK

Received 8 March 2006, in final form 10 April 2006
Published 31 May 2006
Online at stacks.iop.org/PMB/51/3015

Abstract

Phase contrast (PC) imaging is one of the most exciting emerging x-ray imaging techniques, with the potential of removing some of the main limitations of conventional radiology. After extensive experimentation carried out particularly at synchrotron radiation (SR) facilities, the scientific community agrees that it is now time to translate these ideas towards the first clinical implementations. In this framework, a complete model, based on Fresnel/Kirchoff diffraction integrals, was devised. This model accounts for source dimensions, beam spectrum and divergence and detector point spread function (PSF), and can thus be applied to any x-ray imaging system. In particular, by accepting in input the above parameters along with the ones describing the sample, the model can be used to optimize the geometry of the set-up, i.e. to assess the source-to-sample and sample-to-detector distances which maximize feature detection. The model was evaluated by acquiring a range of images of different samples with a laboratory source, and a good agreement was found between simulated and experimental data in all cases. In order to maximize the generality of the results, all acquisitions were carried out using a polychromatic source and an energy-resolving detector; in this way, a range of monochromatic images could be obtained as well as polychromatic images, which can be created by integrating different parts of the acquired spectra. One of the most notable results obtained is that in many practical cases polychromatic PC imaging can provide the same image quality as its monochromatic counterpart. This is an important step in the wider application of PC using conventional sources.

1. Introduction

Among new imaging techniques currently under development, phase contrast (PC) imaging appears to be one of the most promising with respect to improving the state of the art of

diagnostic radiology (Lewis 2004). The technique relies on the phase shift suffered by x-rays when crossing an object, and has been shown to provide increased image contrast compared to conventional techniques based on absorption (Snigirev *et al* 1995, Wilkins *et al* 1996, Arfelli *et al* 1998). After extensive experimentation, carried out mainly at synchrotron radiation (SR) facilities, the scientific community agrees that it is now time to translate these ideas towards the first clinical implementations. This is mainly due to the increased detail detectability observed in several radiological applications, and most notably in the challenging field of mammography (see, for instance, Arfelli *et al* (2000), Pisano *et al* (2000)).

Among the different techniques which can be employed to exploit phase effects, at present the free-space propagation (or 'in-line holography') one appears to be the most suited to a straightforward clinical transfer. In fact the other available phase techniques, namely phase dispersion imaging (Ingal and Beliaevskaya 1995), also called diffraction enhanced imaging (DEI, Chapman *et al* (1997), although the term DEI is referred also to the subsequent application of an image processing algorithm), and x-ray interferometry (Momose *et al* 1996), are based on the use of perfect crystals. Although in some cases they are capable of providing even higher image quality than free-space propagation PC, techniques based on crystals have at least three major drawbacks with regards to their practical implementation. First of all, perfect crystals require high precision alignment (within microradians), and are thus extremely sensitive to environmental vibrations. Secondly, they imply the use of monochromatic beams, which may result in low fluxes when laboratory sources are employed. Finally, crystals absorb a fraction of the beam outcoming from the sample, which means that dose delivery is not optimized.

Moreover, further complications are encountered in the case of interferometry, as interferometers are normally obtained by precise cutting of monolithic crystals, which makes the realization of devices large enough for clinical investigations rather difficult. On the other hand, the fabrication of an interferometer based on three separate crystal blades would be made even more challenging by the necessity of tuning the distances between the different blades within one atomic unit.

All these complications are not encountered when the free-space propagation technique is employed. This technique is based only on the optimization of the source-to-sample and sample-to-detector distances, without requiring any optical element in between. The phase signal arises from the interference between differently shifted wave fronts, which gives rise to fringes along the edges of the details contained in the sample. As discussed below, provided the set-up is optimized these fringes are detectable, and they enhance the visibility of all details in the image.

Free-space propagation phase contrast images with polychromatic beams were already obtained in the past (see, for instance, Wilkins *et al* (1996)). The current work proves that in most practical cases the fringe intensity obtainable with a polychromatic spectrum is fully comparable to the one that would be obtained with an equivalent energy monochromatic beam. This provides a fundamental step towards practical (i.e. with laboratory sources) implementations of the technique, as the full photon flux is available to create the image.

A classical and reliable way to model the PC image formation mechanism is provided by Fresnel/Kirchoff diffraction integrals. This approach is described in standard text books (Born and Wolf 1980, Cowley 1975), and has been followed in the work of Snigirev *et al* (1995) and Arfelli *et al* (1998). It allows a precise prediction of the pattern that would be generated by a monochromatic point source and recorded with a detector with infinite spatial resolution (we will refer to this as the 'pure' pattern I in the following). The way in which source size (i.e. partial spatial coherence) and detector finite resolution have to be taken into account has been considered in the work of Arfelli *et al* (1998), and further discussed in Olivo

(2005) and in Peterzol *et al* (2005). Basically, the 'pure' pattern has to be convolved with the detector point spread function (PSF) and with the rescaled source distribution. The latter is obtained from the division of the object-to-detector (z_{od}) by the source-to-object distance (z_{so}),

$$J = I * \mathrm{PSF} * \left[S \frac{z_{od}}{z_{so}} \right] = I * \mathrm{PSF} * s \tag{1}$$

where J is the acquired pattern, S the source distribution, $*$ the convolution operator and s is the rescaled source distribution. By exploiting the properties of the convolution, it is in many cases more practical to first convolve the PSF with s

$$f = \mathrm{PSF} * s \tag{2}$$

and then to obtain J by convolving the obtained curve f with the pure pattern I. Obviously, an equivalent approach would consist in multiplying the Fourier transforms of f and of the 'pure' pattern and inverse-transforming the result,

$$J = F^{-1}[F(I)F(f)] \tag{3}$$

where F and F^{-1} indicate the direct and inverse Fourier transform operators, respectively. The result of these convolutions is smearing of the pattern fine features and a consequent reduction of the intensity of first minima and maxima, the effect being more dramatic as the curve described by f becomes wider. This implies the necessity of finding a trade-off magnification of the system that optimizes image quality. For example, a too short sample-to-detector distance would result in very narrow fringes, possibly narrower than the detector PSF and thus almost undetectable. If on the other hand the sample-to-detector distance is made too large, s would be increased accordingly, and the resulting large width of f might smear out the pattern completely. In the present paper, the effect of the beam polychromaticity (partial temporal coherence) has also been taken into account.

An alternative, simplified approach is provided by the ray tracing techniques, in which each x-ray is followed along its path through the sample, and the deviation from its original propagation direction is calculated via the gradient of the projected phase shift introduced by the sample. This approach was followed for instance by Davis *et al* (1995). Although this kind of approach does not allow the estimation of secondary fringes, in most practical cases the effect of the source and detector convolutions is a complete disappearance of all minima and maxima except the primary ones, and thus this approximation can often be used effectively. A detailed discussion of the transition between Fresnel/Kirchoff and ray tracing approaches, and of the validity limits of the latter, can be found in Peterzol *et al* (2005).

Finally, a new interesting approach was developed by Wu and Liu (2004), in which the Wigner distribution formalism is used to take the partial coherence into account. In the same work, the partial coherence of an anode source is assessed by means of the Van Cittern–Zernike theorem, and an overall parameter expressing the phase contrast potentials of an imaging system, which the authors call *relative phase contrast factor*, is obtained (see also Wu and Liu (2003)). A first experimental verification of this model was provided by Donnelly *et al* (2005) by exploiting previously collected data.

In this paper, however, the classic Fresnel/Kirchoff formalism outlined above has been followed which allowed us to focus on the intensity of the PC signal produced by a given sample, and to separately assess the effects of source size, detector PSF and beam polychromaticity on this intensity. Provided that source distribution, x-ray spectrum and detector PSF are known, the model holds for any imaging system, and it can therefore be used to determine the set-up (i.e. source-to-sample and sample-to-detector distance) which maximizes the signal intensity for a given sample.

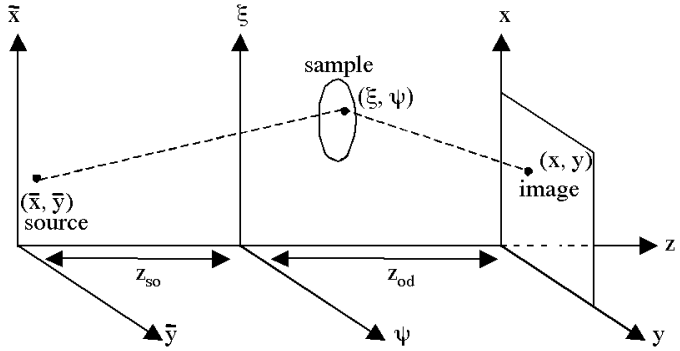

Figure 1. Layout of the generic experimental set-up used in 'in-line holography' or 'free-space propagation' phase contrast imaging.

There is a significant and growing interest in polychromatic PC imaging. After the first attempts at medical PC imaging with conventional sources (Kotre and Birch 1999, Donnelly and Price 2002), Konica-Minolta has commercialized the first mammography system exploiting image enhancement due to phase effects[1], and the use of novel sources (Krol *et al* 1997, Gaudin *et al* 2001) has recently been considered for PC imaging applications as well (Toth *et al* 2005).

2. Materials and methods

2.1. The simulation

The core of the simulation is a routine which solves the Fresnel/Kirchoff diffraction integrals numerically. Both the integrals and the way of modelling the phase shift due to a simple object have been discussed in detail in previous papers (Snigirev *et al* 1995, Arfelli *et al* 1998, Olivo 2005), and thus only the very basic formulae will be given here, with figure 1 as a frame of reference.

In order to evaluate the electric field due to the source on the image plane, one has to solve the following integral,

$$E(x, y) = -\frac{\mathrm{i}\cos\theta}{\lambda}\int_{-\infty}^{+\infty}\mathrm{d}\xi\int_{-\infty}^{+\infty}\mathrm{d}\psi\, F(\xi, \psi) \tag{4}$$

with

$$F(\xi, \psi) = \frac{\exp\left(\frac{2\pi\mathrm{i}}{\lambda}\left\{\left[z_{\mathrm{so}}^2 + (\bar{x}-\xi)^2 + (\bar{y}-\psi)^2\right] + \left[z_{\mathrm{od}}^2 + (\xi - x)^2 + (\psi - y)^2\right]\right\}\exp[\mathrm{i}\phi(\xi, \psi)]\right)}{\sqrt{\left[z_{\mathrm{so}}^2 + (\bar{x}-\xi)^2 + (\bar{y}-\psi)^2\right]\left[z_{\mathrm{od}}^2 + (\xi - x)^2 + (\psi - y)^2\right]}} \tag{5}$$

where θ is the inclination factor, i the imaginary unit, λ the radiation wavelength and $(\bar{x}, \bar{y})$, (ξ, ψ) and (x, y) are the transverse spatial coordinates in the source, object and image planes, respectively (see figure 1). The phase shift due to the imaged object is expressed by the term ϕ, which can be obtained as

$$\phi(x, y) = -\frac{2\pi}{\lambda}\int_{\mathrm{object}}\delta(x, y, z)\,\mathrm{d}z \tag{6}$$

[1] http://konicaminolta.com/research/core_technology/mi_001.html.

where δ is the decrement from unity of the real part of the refractive index of the object. Thus, to obtain the electric field in a given point (x, y) of the image plane, all possible paths connecting the source to that point via any possible point of the object plane are taken into account, and the appropriate phase shift is applied to all paths going through the object.

It is important to note that the passage from parallel to diverging beam has already been introduced in the above formulae, as the spherical wave $\exp(\mathrm{i}\,\mathbf{k}r)/r$ has been used instead of the plane one $\exp(\mathrm{i}\,\mathbf{k}r)$, where $\mathbf{k}$ is the wave vector and r the distance from the source. This corresponds to the introduction of the denominator in formula (5), in which r does not appear explicitly as the integral is extended over all source to image plane trajectories via any point in the object plane.

Moreover, in order to take the sample absorption into account, it is necessary to use the complex form of the refractive index

$$n = 1 - \delta + \mathrm{i}\beta \tag{7}$$

when solving the integrals, i.e. to replace δ with $\delta - \mathrm{i}\beta$ in equation (6). Once the integration has been carried out, the 'pure' pattern, I, is obtained as the square modulus of the electric field provided by equation (4):

$$I(x, y) = |E(x, y)|^2 . \tag{8}$$

Although there are several interesting examples in the literature showing that the integrals can be solved analytically by assuming certain simplifying conditions (see, for instance, Pogany *et al* (1997)), in the current work the integrals have been solved numerically. In this way no restrictive conditions have to be imposed, with the exception of the very general ones which have to be introduced to derive the integrals themselves, as discussed by Born and Wolf (1980).

The integration provides the 'pure' intensity I at one point of the pattern, so that the process has to be repeated for a number of times equal to the required length of the vector which will contain the pattern. When imaging a 100 μm fibre (see section 3), the interference pattern extends over about 300 μm, and thus 300 points were chosen with a 1 μm step. Smaller sampling steps are not required as all patterns have to be convolved with the curve f, which has a FWHM of a few tens of μm in all practical cases. The measurements of s and of the PSF, the convolution of which provides f, will be discussed in sections 3.1 and 3.2 respectively. All convolutions are performed numerically by means of a simple routine. The result of the convolution between I and f is J^{mono}, a pattern describing the signal that would be obtained with the same detector and source distribution if the source were monochromatic. As shown in section 3.4, this pattern can be obtained by using the polychromatic source in conjunction with an energy-resolving detector.

The measurement of the source spectrum will be discussed in section 3.1. The optimal spectrum binning was assessed by comparing monochromatic patterns obtained with neighbouring energies. It was observed that an energy binning of 0.5 keV is sufficient for our purposes, as shown in figure 2.

Thus all spectra used in this analysis were re-binned to 0.5 keV energy intervals and then normalized so that the single spectral entries could be used as weighting factors.

Given certain experimental conditions (i.e. source-to-sample and sample-to-detector distances), the above routine was used to generate 'pure' monochromatic patterns I^{mono} in 0.5 keV steps at all energies included in the spectrum. In the case of mutually incoherent waves of different energies, the incoherent sum of the intensities has to be undertaken, instead of the coherent sum of the amplitudes (Born and Wolf 1980). In order to achieve this, the

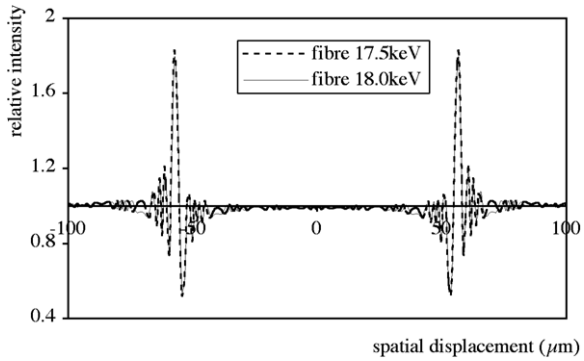

Figure 2. Monochromatic 'pure' patterns (see text) at 17.5 (dotted line) and 18 keV (solid line). As it can be seen, even though the patterns have not yet been convolved with f (see text) and all the fine features are still present, the difference between the two is negligible. In this example, a 100 μm diameter polyethylene fibre placed at 2 m from the source and with a fibre-to-detector distance of 0.2 m was simulated.

normalized spectral entries were used to obtain the polychromatic pattern I^{poly} as a weighted sum of the monochromatic ones,

$$I^{\text{poly}} = \sum_{k=1}^{N} w_k I_k^{\text{mono}} \tag{9}$$

where w_k are the normalized spectral entries. I^{poly} was then convolved with f to obtain J^{poly}, which takes into account the effects of limited spatial coherence and detector resolution and thus represents the pattern which will actually be acquired experimentally. It is important to note that, due to the commutative properties of summing and convolution, the order in which the last two steps are carried out is not important. Thus, by first convolving each single monochromatic pattern with f, and then weighted-summing the convolutions according to the spectral entries, exactly the same result is obtained, i.e.,

$$J^{\text{poly}} = I^{\text{poly}} * f = \left(\sum_{k=1}^{N} w_k I_k^{\text{mono}}\right) * f = \sum_{k=1}^{N} w_k \left(I_k^{\text{mono}} * f\right) = \sum_{k=1}^{N} w_k J_k^{\text{mono}}. \tag{10}$$

In this paper, the first approach was followed as it requires a single convolution operation and is therefore less time-consuming.

2.2. The source

The source is a prototype fine-focus, molybdenum target mammography source designed and manufactured by X-Tek systems Ltd[2], Tring, UK. It features a 1 mm thick aluminium exit window, which removes the low spectral components, and a filter holder. Although normally operated with 30 μm Mo filtration, the filters were removed for this experiment in order to achieve a higher flux. The source can be operated both in fluoroscopy and pulsed mode, but for these experiments it was used in fluoroscopy mode. Focusing and steering magnets are used to optimize the focal spot characteristics, and the magnets' parameters have to be set by the user. As the focal spot size is one of the primary issues in phase contrast imaging, a

[2] http://www.xtekxray.com/.

procedure involving the determination of the FWHM of the focal spot at a range of focusing conditions was devised to optimize the operating parameters.

2.3. The detector

The detector was a liquid nitrogen cooled high-purity Germanium crystal (diameter 16 mm, thickness 13 mm), produced by ORTEC (Oak Ridge, TN, USA), with on-board charge sensitive preamplifier. The rest of the read-out chain consisted of ORTEC amplifier and pulse height analyser modules, controlled by MAESTRO, the ORTEC multi-channel analyser emulation software.

In order to achieve the high degree of spatial resolution necessary to acquire the PC patterns, a 30 μm pinhole (Degussa Ltd, Manchester, UK) was aligned with the centre of the detector entrance window. All other parts of the detector were shielded with lead to ensure that stray photons were not detected. The assessment of the PSF of the 30 μm circular pixel obtained with this arrangement is discussed below (section 3.2).

Using a 30 μm aperture with the HpGe detector, spatial and energy resolution are maximized at the same time, allowing the simultaneous acquisition of monochromatic patterns (obtained, for example, by integrating only the counts in the Kα line of the molybdenum spectrum) as well as all of their polychromatic combinations. This is an essential component of the present study, as one of the aims is to model polychromatic PC and to assess its potentials with respect to the corresponding monochromatic case. Moreover, this arrangement has another advantage which could provide the basis of further developments, as two or more monochromatic patterns can be acquired simultaneously by exploiting different spectral regions (for instance peaks, if available, but in principle at any energy provided the statistics is high enough). As demonstrated by Gureyev *et al* (2001), this enables phase retrieval techniques, which allow the reconstruction of the projected electron density of the sample or even of its 3D rendering in the case of tomographic applications. An alternative approach to enable phase retrieval, developed by Cloetens *et al* (1999), involves taking many monochromatic images at different sample-to-detector distances. The multi-energy approach employed in the current study has the clear advantage that it is sufficient to acquire a single image.

2.4. The set-up

The detector–pinhole combination was placed at 220 cm from the source, and aligned with the beam axis by means of a laser. Once aligned, beam and detector are kept stationary and the PC patterns obtained by horizontally scanning the samples in front of the pinhole. Manually driven micrometric precision translation stages ($\sim$1 μm resolution, Starrett, Athol, MA, USA) were used for sample scanning. Vertically orientated polyethylene fibres (diameters from 100 to 300 μm) were used as samples, held between two fully absorbing sharp copper edges forming a slit with $\sim$800 μm aperture. The purpose of the slit was twofold: firstly it ensured easy sample localization leading to reduced scanning time, and secondly the edges themselves were used to assess the system PSF by scanning them in front of the pinhole (see section 3.2).

The whole sample scanning system was mounted on a support which allowed placing it in different positions along the source–detector axis, in order to acquire patterns in different source-to-sample/sample-to-detector distance combinations. A schematic layout of the experimental set-up is shown in figure 3.

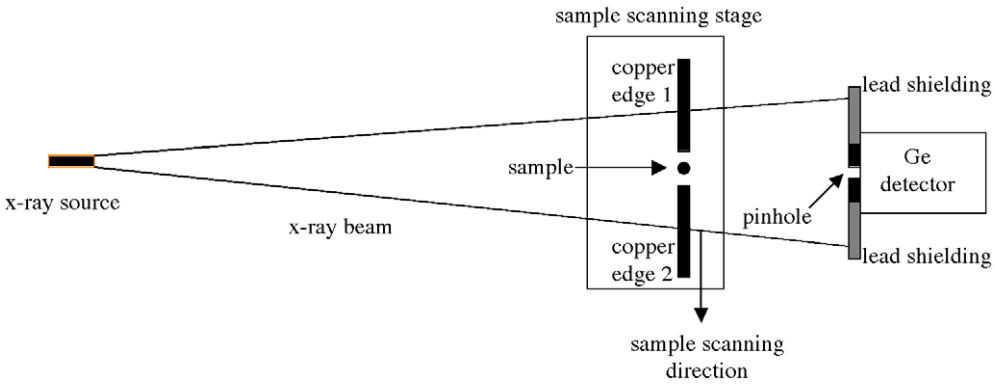

Figure 3. Schematic layout of the acquisition set-up (top view, not to scale).

3. Results and discussion

3.1. Source characterization

A one-off experimental source has been used for this experiment, in which the values of the focusing and steering magnets associated with the electron beam have to be set by the user. In order to find the magnets' parameters corresponding to the optimal focusing, a specific procedure was devised, based on acquiring a range of images of an edge in different configurations, and fitting the results in order to obtain the set of parameters minimizing the edge penumbra.

After the focal spot was optimized, the spectral measurements were carried out. The detector system was calibrated using an ^{241}Am source. The energy resolution was found to be 0.35 keV at 59.5 keV, which was more than sufficient for our experimental requirements. Tube spectra were then acquired at different kVp values (25, 30 and 35), although 35 kVp was almost always used in these experiments, to increase the tube output and reduce the acquisition time. The detector system was operated with less than 10% dead time in all experiments.

All measurements (spectra and PC patterns) were acquired with a source-to-detector distance of 2.2 m, so that the effect of air absorption was constant. Escape peak correction was applied by finding the centre of gravity of the escape peaks, computing the number of escape counts and adding these to the appropriate channels of the spectrum. Although this had some relevance for the 17.4 keV line, the effect was negligible for the 19.6 keV line. An example of a spectrum (35 kVp) is shown in figure 4, in its corrected and uncorrected version. Once corrected all acquired spectra were then re-binned at 0.5 keV and used as inputs to the simulation.

Finally, the full width at half maximum S of the focal spot was assessed. This was done by acquiring a range of edge images at different edge-to-detector distances (z_{ed}), and estimating the width of the penumbra P as a function of distance by means of specifically developed fitting software. The images were recorded on a CCD based camera (Grundig Electronics (now Plettag AG) CCD camera, model FA87, Grundig, Nurnberg, Germany). Once a range of P values was obtained, S was extracted by fitting the linear function

$$P = \frac{S}{z_{se}} z_{ed} \tag{11}$$

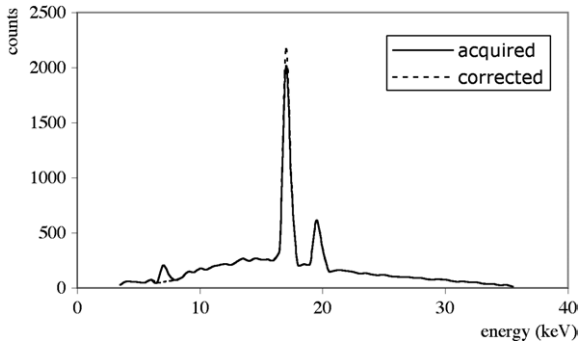

Figure 4. Ge-escape corrected and uncorrected source spectra.

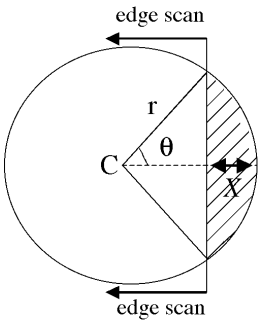

Figure 5. Modelling the ERF of a circular pixel (see text).

where z_{se} is the source-to-edge distance. The PSF of the CCD camera was estimated in advance and taken into account in the evaluation; however, its influence can be made less relevant by increasing the z_{ed}/z_{se} ratio.

The estimated dimension for S was 100 ± 10 μm, which is generally regarded as sub-optimal for PC imaging. Investigations are currently on the way with the source manufacturer, to improve the focusing system in order to achieve a finer focal spot.

However, provided the acquisition set-up is optimized, a focal spot of 100 μm is still small enough to achieve a reasonable PC signal, as shown below (section 3.4).

3.2. Detector system characterization

The detector–pinhole combination provides a single-pixel, energy-resolved, single photon counting detector. As only one pixel is available the samples were scanned in front of the detector to acquire the patterns. However, due to the cylindrical symmetry of the fibres used as samples, a one-dimensional scan was sufficient to achieve all necessary information. For the same reason, the line spread function (LSF) of the pixel was assessed rather than its full PSF. To assess the LSF, the method of deriving the edge response function (ERF) was followed, as the scanned acquisition set-up allowed an easy measurement of the ERF by scanning a fully absorbing edge in front of the pixel (see, for instance, Olivo *et al* (2000)).

A peculiarity of the devised system, however, consists in the fact that the pixel is circular rather than square or rectangular as in conventional detectors. By referring to figure 5, however, it can be seen that, for the edge in a given position, the exposed area A_{exp} (shaded area in the

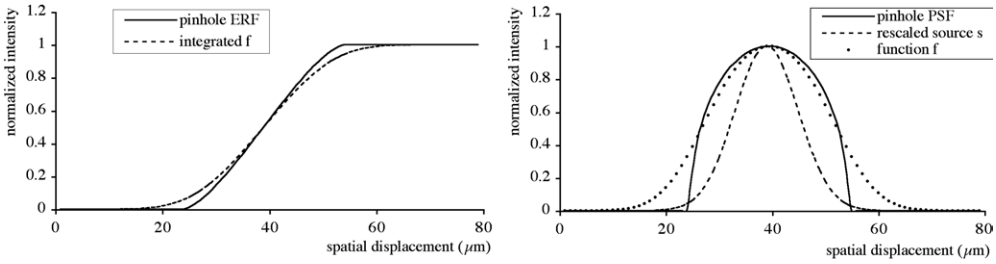

Figure 6. Modelling the f_{INT} function (see text); integral curves are shown on the left-hand side, derivatives on the right-hand one. The solid line on the left is the pinhole ERF obtained by equation (13), i.e., A_{exp}; its derivative (i.e., $\mathrm{LSF}^{\mathrm{pinhole}}$) is the solid curve on the right-hand side. This has to be convolved with s (dashed line on the right) to obtain f (dotted curve on the right). By integrating f, one obtains f_{INT} (dashed curve on the left).

figure) is given by

$$A_{\mathrm{exp}} = r^2(\theta - \sin\theta\cos\theta) \tag{12}$$

where r is the pinhole radius and θ is half the angle subtended by the exposed area. By expressing θ, $\sin\theta$ and $\cos\theta$ as a function of the edge position X, it is then possible to write

$$A_{\mathrm{exp}} = r^2 a\cos\left(\frac{r-X}{X}\right) - (r-X)\sqrt{X(2r-X)} \tag{13}$$

which gives the 'ideal' ERF as a function of the spatial displacement. A good approximation of this 'ideal' ERF would be obtained by scanning the edge as close as possible to the pixel (in our case to the pinhole), in order to make the effect due to s negligible.

In our case, however, we preferred to place the edge in the same position as the samples. With this arrangement, the integral of the function f (equation (2)) can be measured directly. This arrangement is more convenient since f is a primary parameter in the model, representing the function with which the 'pure' pattern I has to be convolved. The model developed up to this point allowed us a relatively straightforward comparison with the experimental data, as the integral of the curve f that one expects in this case (f_{INT}) is obtained by

$$f_{\mathrm{INT}} = \int f(X)\,\mathrm{d}X = \int (\mathrm{LSF}^{\mathrm{pinhole}} * s)\,\mathrm{d}X = \int \left[\left(\frac{\mathrm{d}A_{\mathrm{exp}}}{\mathrm{d}X}\right) * s\right]\mathrm{d}X. \tag{14}$$

As the measurements described in section 3.1 provided an estimate of the source FWHM, rather than of its spatial distribution, the distribution was modelled as a Gaussian function with a FWHM of 100 μm. This assumption is not restrictive in our case. Source-to-sample distances ranging from 184 to 193 cm and sample-to-detector distances from 27 to 36 cm were used in this experiment. As a consequence, the FWHM of s ranged from 14 μm (in the 27 cm/193 cm arrangement) to 20 μm (in the 36 cm/184 cm one). This meant that the resulting FWHM of f was always dominated by the 30 μm FWHM of $\mathrm{LSF}^{\mathrm{pinhole}}$ (when two bell-shaped curves are convolved together, the resulting curve has a FWHM equal to good approximation to the quadrature sum of the two original FWHMs). The entire process (for the 27 cm/193 cm case) is shown in figure 6.

Figure 7 shows the comparison between the theoretical f_{INT} provided by equation (14) and the experimental points obtained by scanning the edge in front of the detector in 10 μm steps, in the source-to-edge = 193 cm/edge-to-detector = 27 cm arrangement. It can be seen that a good agreement is observed. The entire procedure was repeated for the 184 cm/36 cm arrangement, and the same level of agreement was found.

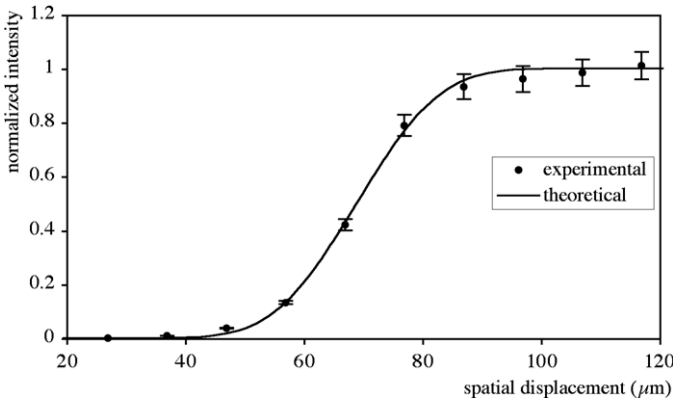

Figure 7. Comparison between the theoretically modelled (solid line) and experimentally sampled (dots) f_{INT} curves (see text).

The derivative of the theoretical function shown in figure 7 (i.e. the dotted curve on the right-hand side of figure 6) can thus be considered a precise, finely sampled estimate of the function *f*. This function (and its 184 cm/36 cm correspondent) was used to convolve the 'pure' PC patterns before comparing them to the experimental data.

3.3. Simulation results

All simulation results are for a 100 μm thick polyethylene fibre imaged with a source-to-detector distance of 220 cm, in two different configurations: source-to-sample distance = 200 cm and sample-to-detector distance = 20 cm (200/20 in the following, shown as solid line in the graphs below) and source-to-sample distance = 180 cm and sample-to-detector distance = 40 cm (180/40 in the following, shown as dashed line in the graphs). The monochromatic case (17.5 keV) and the polychromatic case (35 kVp) are presented and the interplay between the effects due to source size, detector PSF and polychromaticity considered. In all cases the 30 μm pinhole LSF was used to describe the detector, and a 100 μm, Gaussian-distributed source was assumed.

Figure 8 shows the patterns obtained in the monochromatic case (17.5 keV). Pure patterns are shown in figure 8(a): these are the patterns that would be acquired with a point source and with an infinite spatial resolution detector. In this case, the 180/40 combination would be the more advantageous one: the pattern has more space to develop, there is a higher degree of magnification, and as a consequence the main peaks are both higher and broader. If only the effect of the detector is taken into account (figure 8(b): a point source and a 30 μm circular pixel), this would still be the case, as higher and broader peaks are less affected by a convolution with the same function. This suggests that if the effect of the source is negligible with respect to that of the detector, higher sample-to-detector and reduced source-to-sample distances are preferable. This might be a practical case if an ultra-fine focal spot source is used in combination with a detector with a pixel of the order of a few tens of μm.

If, on the other hand, the effect of the detector is negligible with respect to the source, the situation is reversed. This is clearly discernible in figure 8(c), which takes only the effect of the source into account (i.e. it shows the patterns that would be obtained with a 100 μm source and a detector with infinite spatial resolution). This could be the case if a high-resolution film, or a CCD camera with pixels of the order of a few μm, is used in combination with a

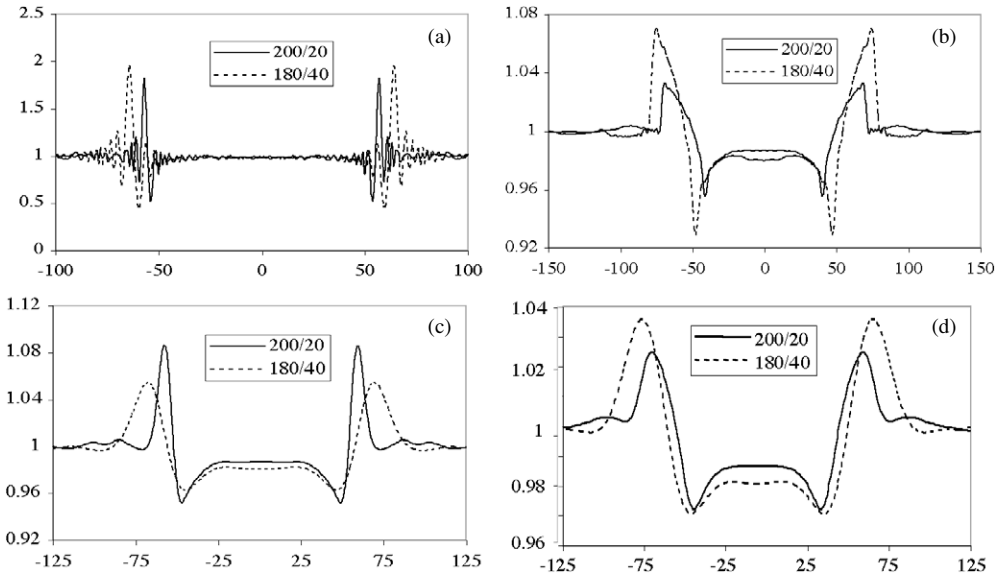

Figure 8. Simulated PC patterns of a 100 μm polyethylene fibre, imaged with 17.5 keV monochromatic radiation in two different source-to-sample/sample-to-detector distance arrangements. (a) 'pure' patterns; (b) effect of the detector alone; (c) effect of the source alone; (d) combined effect of source and detector. In all cases, the relative intensity is given as a function of the spatial displacement in μm. Note that, in order to display patterns of different intensity and width in the same figure, the horizontal and vertical scales have been changed accordingly.

modern mammography source. This shows that as the rescaled source distribution s becomes broader (the 180/40 combination compared to 200/20, i.e., about 22 versus 10 μm), the convolution with the broader function results in a more dramatic smearing of the peaks. Finally, figure 8(d) shows the patterns affected by both the source and the detector, i.e. the pattern expected in the experimental conditions described in the present paper. As discussed above, in our case the effect of the detector dominates over that of the source, and in fact the 180/40 combination is more advantageous. This, however, applies to the specific equipment used in these experiments, and in general the optimal trade-off has to be found according to the relative contributions of source and detector.

In figure 9, the four situations outlined above for the monochromatic case are re-evaluated with the polychromatic spectrum. In this case, the 'pure' patterns (figure 9(a)) are characterized by broader peaks and by a reduced overall number of ripples, due to the superposition of minima and maxima arising from different energy photons in the spectrum. As the relative shift between minima and maxima of the same order created by different energies increases with the peak order, the overall effect is a complete disappearance of high-order peaks, while low-order peaks are generally affected by peak broadening only.

Despite this removal of fine structure, it is interesting to note that the considerations drawn from the monoenergetic case hold also in the polychromatic case, in particular the reduced sample-to-detector distance being more beneficial when the rescaled source size s is broader than the detector PSF and vice versa.

This is due to the fact that the convolution with s and PSF smears out high-order peaks whatever spectral distribution used and thus, the final results are mainly driven by the first-order peaks. As discussed above, the effect of the polychromaticity on primary peaks is that

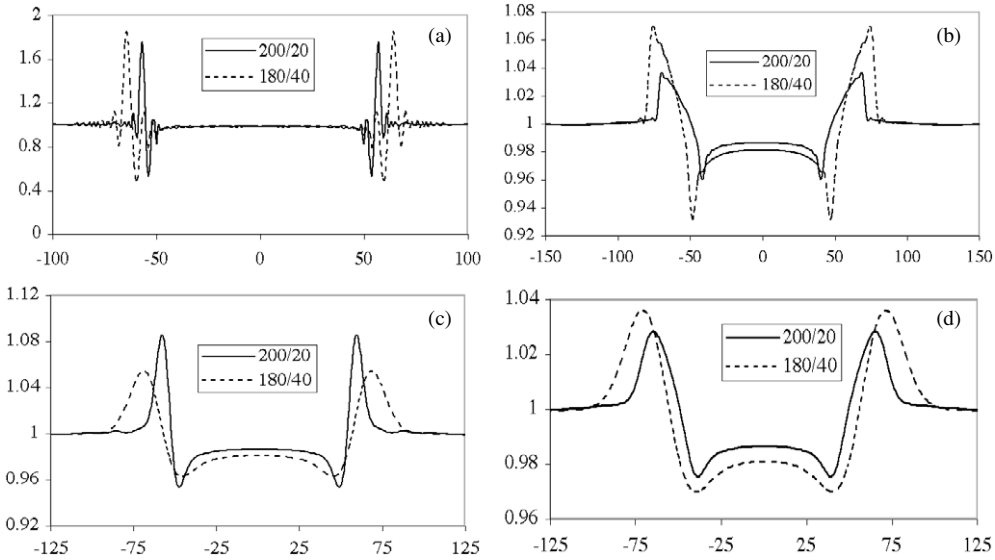

Figure 9. Simulated PC patterns of a 100 μm polyethylene fibre, imaged with polychromatic radiation (spectrum shown in figure 4, energies from 12 to 30 keV) in two different source-to-sample/sample-to-detector distance arrangements. (a) 'pure' patterns; (b) effect of the detector alone; (c) effect of the source alone; (d) combined effect of source and detector. In all cases, the relative intensity is given as a function of the spatial displacement in μm. Note that, in order to display patterns of different intensity and width in the same figure, the horizontal and vertical scales have been changed accordingly.

of broadening, as their relative position changes little with varying energies, and the effect on peak height is not large. For example, moving from monochromatic to polychromatic radiation, in the 'pure' patterns the first maximum goes from relative intensity 1.82 to 1.75 in the 200/20 case and from 1.95 to 1.85 in the 180/40 one. The interesting aspect here is that convolving with the same function two different peaks, one narrower but higher and the other wider but less intense, produces a similar result. In fact, in the 180/40 arrangement, the intensity of the primary peaks of the patterns convolved with source and detector (figures 8(d) and 9(d)) is the same (1.036) in both the monochromatic and the polychromatic case.

This is an extremely important result in this context, as it suggests that polychromatic PC imaging might be able to provide the same results and enhancement of detail in an image as its monochromatic correspondent. An experimental proof of this is shown in section 3.4.

3.4. Validation of the simulation via comparison with experimental data

The experimental set-up described above was used to acquire PC patterns that could be compared to the simulation. 300 and 100 μm thick polyethylene fibres were scanned across the stationary beam, with scanning steps equal to 20 and 50 μm. This corresponds to sampling with the same step the convolution between the 'pure' pattern and the function f. At each step, an entire spectrum was acquired; monochromatic patterns were then obtained by integrating counts only from the Kα peak of the molybdenum spectrum, while the polychromatic patterns were obtained by integrating all counts between 12 and 30 keV. Two different sample-to-detector distances were evaluated, 27 and 36 cm, with corresponding 193 and 184 cm

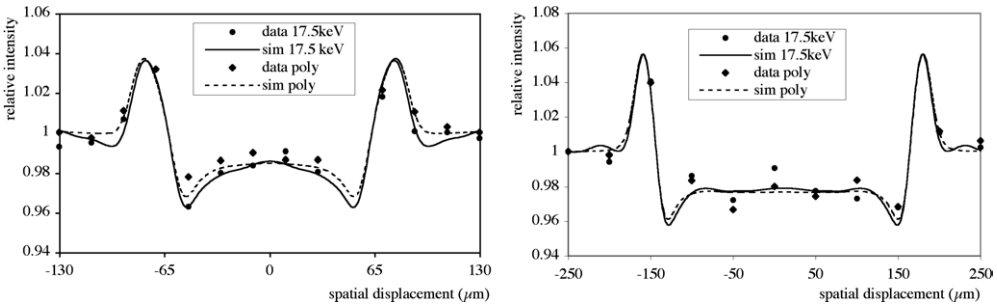

Figure 10. Comparison between simulated and experimental data. In both graphs, the solid line represents the simulated monochromatic pattern, the dashed line the simulated polychromatic one; circles are the monochromatic data and diamonds the polychromatic ones. The 100 μm fibre sampled at 20 μm in the 193/27 arrangement is shown on the left-hand side, while the 300 μm fibre sampled at 50 μm in the 184/36 arrangement is shown on the right-hand one. Error bars ($\sim$0.5%) are not shown to avoid cluttering the figure.

source-to-sample distances in order to maintain the overall source-to-detector distance equal to 220 cm. In accordance with the notation used above, these configurations are referred to as 193/27 and 184/36 in the following.

Figure 10 compares the experimental results with simulations. Two cases in which all parameters are different have been chosen (100 and 300 μm fibres, 20 and 50 μm scanning step, 193/27 and 184/36 arrangements), and it can be seen that the agreement between simulation and experiment is good in all cases. As discussed in section 3.3, the simulated monochromatic and polychromatic patterns are very similar, and the acquired data confirm this result. Analogous comparisons were carried out in all other cases (300 μm fibre in the 193/27 arrangement sampled at 20 and 50 μm, 100 μm fibre in the 184/36 arrangement, etc), and the same agreement was found.

4. Conclusions

A complete model of phase contrast (PC) image formation has been developed. The effects of the source size, of the limited detector spatial resolution, of the beam divergence and polychromaticity have been introduced one at a time in the model, and both their individual and combined effects on the acquired PC signal have been discussed.

In order to check the validity of the model, an experimental set-up in which both energy and spatial resolution are optimized has been devised. The use of an energy-resolved system enabled the simultaneous acquisition of both monochromatic and polychromatic PC patterns, allowing a thorough test of the model in all its different aspects to be carried out. Close agreement between model and experimental measurements was found.

This experimentally verified model allows the prediction of the intensity of the PC signal achievable with any x-ray imaging system (monochromatic or polychromatic, with parallel or divergent x-rays, with any source distribution and employing any detector). As a consequence, it enables the optimization of the set-up, i.e. the determination of the source-to-sample and sample-to-detector distances providing the maximum signal intensity.

The main result from the present study is that the same PC signal intensity can be achieved in many practical cases employing either monochromatic or polychromatic x-rays. This is a fundamental step in ensuring wider practical implementations of the PC imaging technique.

To move from using synchrotron facilities to conventional laboratories or clinical facilities, polychromatic sources must be used in order to avoid excessively long exposure times.

Moreover, the energy-resolved approach to PC pattern acquisition can open the way to phase retrieval techniques in which the acquisition of a single image can be sufficient to reconstruct the projected electron density, or its 3D distributions in the case of a tomographic approach. Similar results obtained in the past required the acquisition of a range of different images (or a range of sinograms in the tomographic case) at different sample-to-detector distances.

Acknowledgments

A Olivo is supported by a Marie Curie Intra-European Fellowship within the sixth European Community Framework Programme, contract no MEIF-CT-2004-009143.

References

Arfelli F *et al* 1998 Low-dose phase contrast x-ray medical imaging *Phys. Med. Biol.* **43** 2845–52

Arfelli F *et al* 2000 Mammography with synchrotron radiation: phase-detection techniques *Radiology* **215** 286–93

Born M and Wolf E 1980 *Principles of Optics* 6th edn (Oxford: Pergamon)

Chapman D, Thomlinson W, Johnston R E, Washburn D, Pisano E, Gmur N, Zhong Z, Menk R, Arfelli F and Sayers D 1997 Diffraction enhanced x-ray imaging *Phys. Med. Biol.* **42** 2015–25

Cloetens P, Ludwig W, Baruchel J, Van Dyck D, Van Landuyt J, Guigay J P and Schlenker M 1999 Holotomography: quantitative phase tomography with micrometer resolution using hard synchrotron radiation x-rays *Appl. Phys. Lett.* **75** 2912–4

Cowley J 1975 *Diffraction Physics* (Amsterdam: North-Holland)

Davis T J, Gao D, Gureyev T E, Stevenson A W and Wilkins S W 1995 Phase-contrast imaging of weakly absorbing materials using hard x-rays *Nature* **373** 595–8

Donnelly E F and Price R R 2002 Quantification of the effect of the kVp on edge-enhancement index in phase-contrast radiology *Med. Phys.* **29** 999–1002

Donnelly E F, Price R R and Pickens D R 2005 Experimental validation of the Wigner distributions theory of phase-contrast imaging *Med. Phys.* **32** 928–31

Gaudin C, Lamoureux M and Rouille C 2001 X-ray emission from a compact hot plasma: applications to radiology and mammography *Phys. Med. Biol.* **46** 835–51

Gureyev T E, Mayo S, Wilkins S W, Paganin D and Stevenson W 2001 Quantitative in-line phase-contrast imaging with multienergy x-rays *Phys. Rev. Lett.* **86** 5827–30

Ingal V N and Beliaevskaya E A 1995 X-ray plane-wave topography observation of the phase contrast from a non-crystalline object *J. Phys. D: Appl. Phys.* **28** 2314–7

Kotre C J and Birch I P 1999 Phase contrast enhancement of x-ray mammography: a design study *Phys. Med. Biol.* **44** 2853–66

Krol A, Ikhlef A, Kieffer J C, Bassano D A, Chamberlain C C, Jiang Z, Pepin H and Prasad S C 1997 Laser-based microfocused x-ray source for mammography: feasibility study *Med. Phys.* **24** 725–32

Lewis R A 2004 Medical phase contrast x-ray imaging: current status and future prospects *Phys. Med. Biol.* **49** 3573–83

Momose A, Takeda T, Itai Y and Hirano K 1996 Phase-contrast x-ray computed tomography for observing biological soft tissues *Nat. Med.* **2** 473–5

Olivo A 2005 Towards the exploitation pf phase effects in clinical synchrotron radiation radiology *Nucl. Instrum. Methods* A **548** 194–9

Olivo A *et al* 2000 Experimental evaluation of a simple algorithm to enhance the spatial resolution in scanned radiographic systems *Med. Phys.* **27** 2609–16

Peterzol A, Olivo A, Rigon L, Pani S and Dreossi D 2005 The effects of the imaging system on the validity limits of the ray-optical approach to phase contrast imaging *Med. Phys.* **32** 3617–27

Pisano E *et al* 2000 Human breast cancer specimens: diffraction-enhanced imaging with histologic correlation – improved conspicuity of lesion detail compared with digital radiology *Radiology* **214** 895–901

Pogany A, Gao D and Wilkins S W 1997 Contrast and resolution in imaging with a microfocus x-ray source *Rev. Sci. Instrum.* **68** 2774–82

Snigirev A, Snigireva I, Kohn V, Kuznetsov S and Schelokov I 1995 On the possibilities of x-ray phase contrast microimaging by coherent high-energy synchrotron radiation *Rev. Sci. Instrum.* **66** 5486–92

Toth R, Kieffer J C, Fourmaux S, Ozaki T and Krol A 2005 In-line phase-contrast imaging with a laser-based hard x-ray source *Rev. Sci. Instrum.* **76** 083701

Wilkins S W, Gureyev T E, Gao D, Pogany A and Stevenson A W 1996 Phase-contrast imaging using polychromatic hard x-rays *Nature* **384** 335–8

Wu X and Liu H 2003 Clinical implementation of x-ray phase-contrast imaging: theoretical foundations and design considerations *Med. Phys.* **30** 2169–79

Wu X and Liu H 2004 A new theory of phase-contrast x-ray imaging based on Wigner distributions *Med. Phys.* **31** 2378–84